The effects of radiative transfer on the reionization of an inhomogeneous universe

Taishi Nakamoto, Masayuki Umemura[★] and Hajime Susa
Center for Computational Physics, University of Tsukuba, Ibaraki 305-8577, Japan

ABSTRACT

Assuming simple dynamics for the growth of density fluctuations, we implement six-dimensional (6D) radiative transfer calculations to elucidate the effects of photon propagation during the reionization of an inhomogeneous universe. The ionizing sources are postulated to be AGN-like in this paper. The present simulations reveal that radiative transfer effects are still prominent considerably after the percolation epoch, in which patchy ionized regions connect with each other. In other words, owing to the collective opacity, the Universe does not become perfectly transparent against ionizing radiation even though strongly self-shielded regions disappear. It turns out that the inhomogeneity of the medium enhances the opacity effects and delays the end of reionization. Owing to such radiative transfer effects, the reionization in an inhomogeneous universe proceeds fairly slowly, in contrast to the prompt reionization in a homogeneous universe, and as a result the surface of reionization is not so sharply edged, but highly uneven. As a signature of the uneven surface of reionization, the cosmic IR background (CIB) radiation, which is produced by Lyα photons resulting from radiative recombination, could exhibit strong anisotropies, reflecting the amplitude of density fluctuations at the reionization era. The predicted CIB intensity lies on a level of possible detection by forthcoming IR space telescope facilities.

Key words: radiative transfer – intergalactic medium – cosmology: theory – diffuse radiation.

1 INTRODUCTION

The cosmic reionization is an issue of great interest in relation to the formation of the first luminous objects, say Population III stars or primordial active galactic nuclei (AGNs), and also the subsequent galaxy formation (Couchman & Rees 1986; Shapiro 1986; Shapiro & Giroux 1987; Tegmark & Silk 1994; Fukugita & Kawasaki 1994; Giroux & Shapiro 1996; Ostriker & Gnedin 1996; Sasaki & Umemura 1996; Gnedin & Ostriker 1997; Haiman & Loeb 1997; Nakamoto, Umemura & Susa 1997; Haiman & Loeb 1998; Miralda-Escudé & Rees 1998; Norman, Paschos & Abel 1998; Abel & Haehnelt 1999; Abel, Norman & Madau 1999; Gnedin 2000; Haiman & Loeb 1999a,b; Madau, Haardt & Rees 1999; Razoumov & Scott 1999; Umemura, Nakamoto & Susa 1999; Valageas & Silk 1999; Ciardi et al. 2000a; Miralda-Escudé, Haehnelt & Rees 2000; Kitayama et al. 2000; Susa & Kitayama 2000). It is widely believed that the event of cosmic reionization took place during the so-called dark age of the Universe, say redshifts $z > 5$, because the absorption by the neutral intergalactic medium (IGM) is observed to be feeble at $z \lesssim 4$, as indicated by the shallow Gunn–Peterson trough (Gunn & Peterson 1965;

Schneider, Schmidt & Gunn 1991) and also because the continuum depression increases steeply up to $\gtrsim 0.8$ at $z \approx 5$ (Dey et al. 1998; Spinrad et al. 1998; Weymann et al. 1998; Stern et al. 2000).

The density fluctuations that originate in the early Universe develop into non-linear density enhancements during the dark age. Because of the high cosmic density at these epochs, the dense regions might be shielded from ionizing radiation. Thus, in order to explore the reionization history, one should invoke radiative transfer in an inhomogeneous universe. The radiative transfer equation is the Lorentz-transformed Boltzmann equation for the photon distribution function in the phase space. Thus, it has in principle six degrees of freedom in three-dimensional space, excluding the dimension of time. There are basically two versions of strategy to pursue the propagation of radiation in a clumpy universe. One is to solve the radiative transfer in an inductively settled clumpy universe in which discrete intergalactic clouds are distributed to satisfy the statistics of Lyman alpha absorption lines seen in QSO spectra. In this case, the problem has been often reduced to time-dependent *one-dimensional* cosmological radiative transfer (Madau 1995; Haardt & Madau 1996; Giroux & Shapiro 1996; Madau et al. 1999). The other strategy is to consider multidimensional radiative transfer in a deductively built-up

[★] E-mail: umemura@rccp.tsukuba.ac.jp

perturbed universe based upon a cosmological scenario. Recent attempts for solving multidimensional radiative transfer are classified into four types of calculations. These are three-dimensional (3D) calculations with the diffusion approximation (Norman et al. 1998) or the local optical depth approximation (Gnedin 2000), photon-conserving radiative transfer (Abel et al. 1999), frequency-independent five-dimensional (5D) calculations (Razoumov & Scott 1999) and frequency-dependent six-dimensional (6D) calculations (Nakamoto et al. 1997; Umemura et al. 1999; Ciardi et al. 2000b).

In an inhomogeneous universe, the reionization is expected to proceed in an outside-in fashion. First, underdense regions are ionized and percolate, leaving overdense neutral islands owing to the self-shielding. Secondly, the ionized sea encroaches into the neutral islands to end up with the overall reionization of the universe. In this paper, assuming simplified dynamics for the growth of density fluctuations, we attempt to solve the full six-dimensional radiative transfer for ionizing photons in an inhomogeneous universe. Attention is focused on elucidating the effects of the radiative transfer on such inhomogeneous reionization processes. We restrict ourselves here to AGN-like ionizing sources. We find that the radiative transfer effects are still emergent even after the overall ionization of the universe, and the inhomogeneity of the medium enhances the the radiative transfer effects. In Section 2, the method for simulations is described. In Section 3, the reionization history in an inhomogeneous universe is presented, and the radiative transfer effects are analysed. Also, we discuss the highly uneven surface of reionization and assess the resultant anisotropies in the cosmic near IR background produced by Lyα photons resulting from radiative recombination. Section 4 is devoted to the conclusions.

2   METHOD

2.1   Numerical model

We consider cosmic reionization in the context of a standard cold dark matter (CDM) cosmology. The density parameters are set to be $\Omega_{CDM} = 0.95$ for CDM and $\Omega_b = 0.05$ for baryons. The density fluctuations are normalized by the present amplitude at $16 h_{50}^{-1}$ Mpc, say $\sigma_8 = 0.6$ (White, Efstathiou & Frenk 1993), where h_{50} is the present Hubble constant in units of $50 \, \text{km} \, \text{s}^{-1} \, \text{Mpc}^{-1}$ ($h_{50} = 1$ in this paper). The CDM cosmology itself is fluctuating as the results of cosmic microwave background anisotropies are updated (Bunn & White 1997). We leave for elsewhere the analyses of the dependence upon a variety of CDM cosmologies. The evolution of the inhomogeneity is represented by generating random Gaussian density fields based upon the Zel'dovich approximation. Here, we should pay attention to spatially resolving fast growing small-scale fluctuations, because they must be significant for local self-shielding in a bottom-up scenario like a CDM cosmology. Previous analyses have shown that even under the UV background at a level of 10^{-23}–$10^{-21} \, \text{erg} \, \text{s}^{-1} \, \text{cm}^{-2} \, \text{Hz}^{-1} \, \text{sr}^{-1}$ at the Lyman limit, density fluctuations with masses of $\gtrsim 10^8 \, M_\odot$ can collapse (Umemura & Ikeuchi 1984; Thoul & Weinberg 1996; Kitayama & Ikeuchi 2000; Kitayama et al. 2000). To resolve this scale, we consider a rather small comoving volume of $(8 h_{50}^{-1} \, \text{Mpc})^3$ with 128^3 grids. The whole computational domain contains $2 \times 10^{12} \, M_\odot$ baryons and each cell has $1 \times 10^6 \, M_\odot$ baryons on average. We assume that the gas is primordial, consisting of hydrogen and helium. The number ratio of hydrogen to helium is set to be 9:1.

We may eliminate the cosmological terms in the transfer equation, because we consider a relatively small volume. The cosmological redshift difference during the travel of light across this volume is

$$\Delta z = 1.3 \times 10^{-3}(1 + z)^{3/2} R_8, \tag{1}$$

where R_8 is the comoving linear size of the simulation box in units of $8 h_{50}^{-1}$ Mpc. At $z \lesssim 16$, this is smaller than the width of the Lyman continuum by radiative recombination,

$$\Delta z_{rec} \sim \left(\tfrac{3}{2}kT\right)/h\nu_L = 9.5 \times 10^{-2}T_4, \tag{2}$$

where T_4 is the gas temperature in units of $10^4 \, \text{K}$.

In the present calculation, we cannot really determine the accurate temperature, because the density fluctuations are only provided by the Zel'dovich approximation, which does not allow us to calculate the thermal history. In this paper, by taking into account the fact that the equilibrium temperature is $T_4 = O(1)$ in the photoionized plasma (Umemura & Ikeuchi 1984; Thoul & Weinberg 1996), the gas temperature is assumed to be spatially and temporally constant, $T_4 = 1$. However, one should still keep in mind that the temperature dependence of the recombination rate could alter the ionization structure perceptibly (e.g. Abel & Haehnelt 1999). The ionization degrees of H and He are calculated assuming ionization equilibrium between the photoionization, the collisional ionization and the recombination.

2.2   Radiative transfer

If one is interested in the propagation of ionization front, the time-derivative term should be left in the transfer equation (Razoumov & Scott 1999). However, here we concentrate on the final equilibrium state at each redshift, which is achieved during a relatively short time-scale,

$$R/c(1 + z) = 2.6 \times 10^7 \, \text{yr} \, (1 + z)^{-1} R_8 \, h_{50}^{-1}. \tag{3}$$

When this is compared with the cosmic time, $1.33 \times 10^{10} \, \text{yr}$ $(1 + z)^{-3/2} \, h_{50}^{-1}$, we may drop out the time-derivative term and solve the steady transfer equation;

$$\boldsymbol{n} \cdot \nabla I_\nu = -(\kappa_{abs} + \kappa_{sca})I_\nu + \kappa_{sca} \int I_\nu \, d\omega/4\pi, \tag{4}$$

where I_ν is the specific radiation intensity, and κ_{abs} and κ_{sca} are respectively the absorption and scattering coefficients. The recombination photons for hydrogen and helium potentially participate in further ionization of hydrogen. This virtual scattering process makes the transfer equation an integro-differential equation for the recombination line frequencies. Hence, in order to obtain the self-consistent radiation fields, it is necessary to invoke some iterative method. The transfer for each line frequency is solved by the *short characteristics* method (Kunasz & Auer 1988; Stone, Mihalas & Norman 1992), and the radiation fields and the ionization state of the system are converged to by a so-called Λ iteration (see Appendix A). On the other hand, the ionization by the continua is analytically integrated in terms of the incomplete Gamma function (Tajiri & Umemura 1998). For gas of hydrogen and helium, we have developed a novel method, where by treating six frequencies of recombination lines the frequency-dependent radiative transfer is solved with an accuracy of less than 10 per cent (see Appendix B). This new technical contrivance has enabled us to solve the 6D radiative transfer in practical computational time. Combined with the radiative transfer solver,
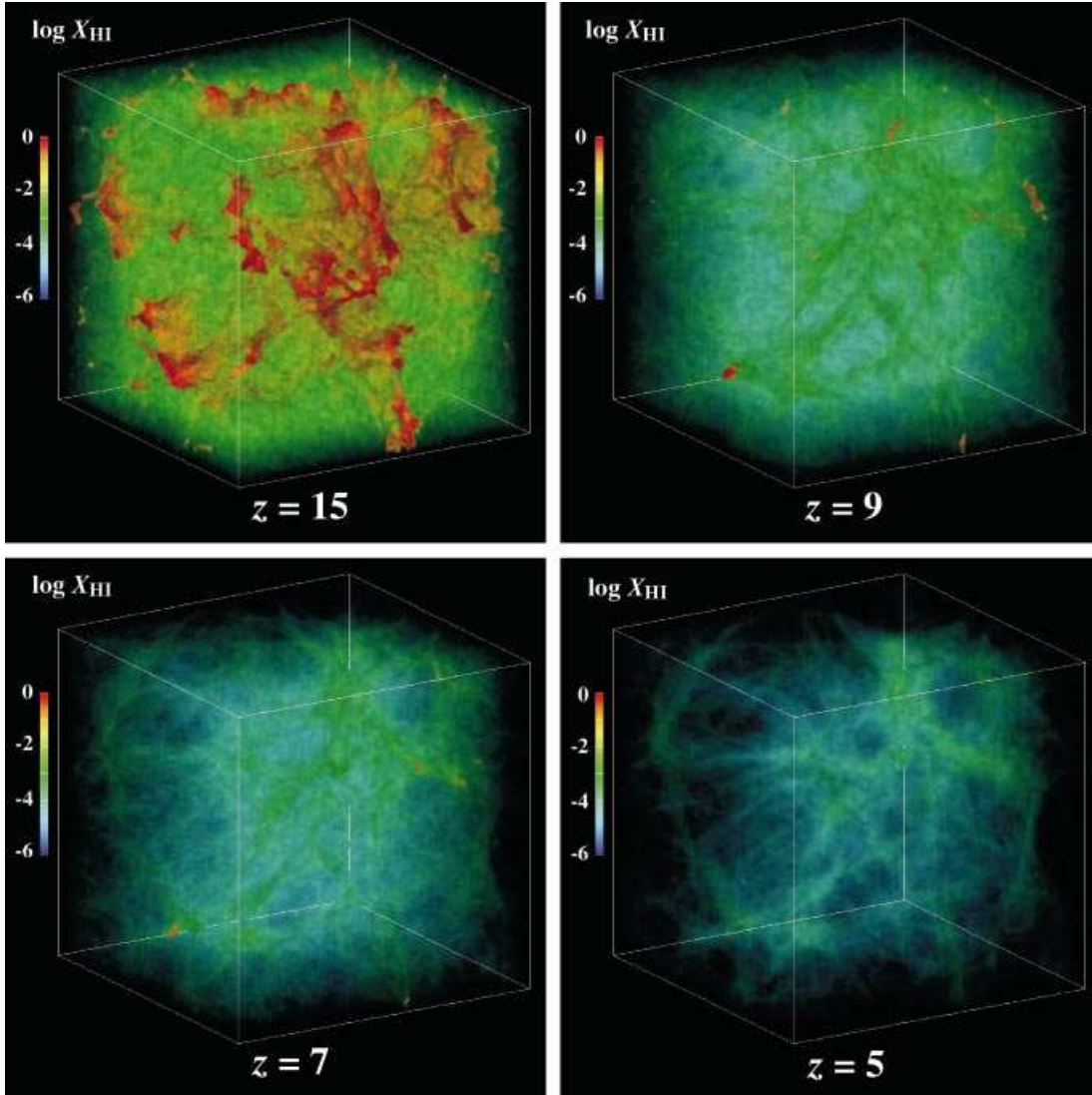
Figure 1. The ionization structure at $z = 15, 9, 7$ and 5 in the case of $J_{21} = 0.1$. The levels of neutral fraction (X_{HI}) in logarithmic scales are shown by colours according to the attached colour bar. At $z = 15$, underdense regions are first reionized and then percolate leaving filamentary neutral overdense regions. After this epoch, the filamentary self-shielded regions are reionized in turn with time. At $z = 7$ all regions are ionized but the radiative transfer effects are still present for the local ionization degree. At $z = 5$ the universe is perfectly transparent against the ionizing radiation.

the ionization rate equation for hydrogen and helium is simultaneously solved. Here, the ionization equilibria are quickly achieved, because the ionization or recombination time-scale is shorter than the cosmic expansion time-scale at redshifts of present interest ($z \gtrsim 4$). The radiative transfer and ionization calculations are repeated until all the physical quantities are converged to with 10^{-4} accuracy.

In the present calculations, we use 128^3 grids for space, 128^2 grids for directions and six grids for frequencies, so that the total number of operations amounts to 1.5 Tflop h ($1\,500$ Gflop h) to obtain the ionization structure at each redshift. To perform 6D radiative transfer calculations, we employ one of highest performance supercomputers, the CP-PACS (Computational Physics by Parallel Array Computer System) at the University of Tsukuba, Japan, which is a massively parallel computer, composed of $2\,048$ processing units, with the theoretical peak speed of 614 Gflop (giga-flops) (Iwasaki 1998). For the present purpose, we have parallelized the radiative transfer solver by a newly developed wavefront method, which is optimized for massively parallel machines (Nakamoto 1999; see the detail in Appendix A).

2.3 Photoionizing sources

The reionization process depends upon the nature and evolution of ionizing sources during the dark age. However, what primarily ionized the Universe during the dark age has remained unsolved observationally as well as theoretically. There are basically two possibilities; one is a first generation of stars in protogalactic condensations (Couchman & Rees 1986; Fukugita & Kawasaki 1994; Ostriker & Gnedin 1996; Gnedin & Ostriker 1997; Haiman & Loeb 1997; Miralda-Escudé & Rees 1998), and the other is low-luminosity AGNs, sometimes called mini-quasars (Tegmark & Silk 1994; Sasaki & Umemura 1996; Haiman & Loeb 1998; Valageas & Silk 1999). Recently, Madau (2000) argued that if stellar sources are responsible for photoionizing the IGM at $z \approx 5$, the star formation rate (SFR) at this epoch must be comparable to or greater than the one inferred from optical observations at $z \approx 3$.

Nonetheless, there is still appreciable uncertainty about the evolution of the SFR at such high redshift epochs (Haiman & Loeb 1999b). In fact, recent submillimetre observations from SCUBA indicate the existence of a substantial population of dust-enshrouded star-forming galaxies (Barger, Cowie & Snaders 1999). On the other hand, Haiman & Loeb (1998) have explored the possibility of reionization by low-luminosity quasars, and found a model consistent with the observed quasar luminosity function. Also, Valageas & Silk (1999) has concluded that a population of faint quasars is needed in order to satisfy all of the recent observations of Lyα clouds, the quasar number count and the helium opacity.

Although both possibilities for ionizing sources are of reasonable interest, we here restrict ourselves to AGN-like sources. Therefore, the frequency dependence for a uniform background radiation is simply assumed to be $J_\nu = J_{\nu_L}(\nu_L/\nu)$, where ν_L is the Lyman limit frequency. At redshifts less than 4, the metagalactic UV background radiation is inferred to be at a level of $10^{-21 \pm 0.5}\,\mathrm{erg\,cm^{-2}\,s^{-1}\,Hz^{-1}\,sr^{-1}}$ from the 'proximity effect' of Lyα absorption lines (Bajtlik, Duncan & Ostriker 1988; Giallongo et al. 1996) and the intensity can be accounted for by the QSO contribution (Haardt & Madau 1996). No information, however, is hitherto available at higher redshifts. The intensity could be significantly lower owing to the rapid evolution of quasar luminosity function (Pei 1995), although it depends upon the size of a faint AGN population. Taking these situations into consideration, we investigate the range of UV intensity as $10^{-3} \le J_{21} \le 1$, where J_{21} is the mean intensity at the hydrogen Lyman edge in units of $10^{-21}\,\mathrm{erg\,cm^{-2}\,s^{-1}\,Hz^{-1}\,sr^{-1}}$.

The reionization of the Universe begins with the development of cosmological H II regions, say Strömgren spheres, around ionizing sources (Shapiro 1986; Shapiro & Giroux 1987). Thereafter, the ionized regions percolate, leaving neutral domains which are exposed to metagalactic UV radiation. We conceive such an intergalactic space as sufficiently far from each ionizing source and therefore impervious to the proximity effects. In other words, we consider a domain irradiated by isotropic UV radiation without placing any ionizing source therein. So, we assume J_{21} in all directions as boundary values on the 3D cube.

3   NUMERICAL RESULTS

3.1   Radiative transfer effects on the reionization

In Fig. 1, the resultant ionization structure is shown at four different epochs, $z = 15, 9, 7$, and 5. Here, the same UV intensity, $J_{21} = 0.1$, is assumed at each redshift. At $z = 15$, the ionization structure exhibits a patchy pattern, where highly ionized underdense regions connect with each other and a network of low-ionized overdense regions is left. At this stage, the central parts of the overdense regions are strongly self-shielded against ionizing radiation, forming neutral cores. Thereafter smaller-scale density fluctuations grow in the linear regime. Then, the absolute densities of overdense regions still decrease with time roughly in proportion to $(1 + z)^2$. Thus, the UV radiation penetrates the overdense regions gradually and the filamentary self-shielded regions are reionized in turn with time. At $z = 9$, the self-shielded neutral regions disappear. At $z = 7$, the whole of each region is highly ionized, but the radiative transfer effects are still present for the local ionization degree as described below in detail. At $z = 5$, the universe is perfectly transparent against the ionizing radiation.

The radiative transfer effects are more directly demonstrated in

Fig. 2, where the local neutral fraction (X_{H_I}) is shown versus the local hydrogen number density (n_H). If the ionizing radiation penetrates the volume freely, the neutral fraction is determined solely in terms of the local density as $X_{H_I} = 0.18 n_H X_e^2 J_{21}^{-1}$, where X_e is the electron fraction. However, the resultant X_{H_I} at $z = 15$ deviates from the prediction in the perfectly transparent (optically thin) medium not only in overdense regions but also in underdense regions. The strongly self-shielded dense cores are clearly shown. The low-density regions by themselves do not have potentiality for the self-shielding. Nonetheless, the neutral fractions there are considerably higher than expected for an optically thin medium. This is because the ionizing radiation is reduced by the collective opacity by surrounding numerous translucent regions. Such effects are also not negligible after strongly self-shielded regions disappear around $z = 7$. As a result, it has turned out that the radiative transfer effects are still important even when the mean neutral fraction is at a level of 10^{-3}. In the present case, at $z \approx 6$ the universe becomes perfectly transparent to ionizing radiation as shown in Fig. 2. Therefore, if we define the end of reionization to be the epoch when the universe becomes perfectly transparent to ionizing radiation, it is concluded that the reionization process in an inhomogeneous universe is not a prompt but a fairly slow event. In other words, we cannot define the surface of reionization to be a sharply edged surface such as supposed in homogeneous reionization (Haiman & Loeb 1999a).

In Fig. 3, with changing the UV intensity in the range of $10^{-3} \le J_{21} \le 1$, the spatial mean of the resultant neutral hydrogen fraction is shown against redshifts, and it is compared with an optically thin approximation. The discrepancy between the full radiative transfer calculations (thick solid curves) and the optically thin approximation (thin dotted lines) reflects the level of the radiative transfer effects. The epoch when both curves come closer to each other roughly gives the end of reionization. Also, for comparison, the result of the radiative transfer calculation for a perfectly *homogeneous* medium is shown by a thin curve only for $J_{21} = 0.1$. A previous analysis (Tajiri & Umemura 1998) has shown that the self-shielding of a uniform cloud vanishes because of the permeation of ionizing photons when the cloud density lessens below

$$n_{\text{shield}} = 1.4 \times 10^{-2}\,\mathrm{cm^{-3}}\ (M_H/10^8\,M_\odot)^{-1/5} J_{21}^{3/5}, \quad (5)$$

where M_H is the cloud mass in hydrogen. If the overall reionization epoch is estimated in terms of n_{shield}, the reionization redshift z_{reion} can be predicted by a condition $\langle n_H(z) \rangle = n_{\text{shield}}$, where $\langle n_H(z) \rangle$ is the average hydrogen density at redshift z. The condition gives $1 + z_{\text{reion}} \simeq 17.6(10 J_{21}/R_8)^{1/5}$. The numerical result for homogeneous medium is in good agreement with this estimate. However, we see a noticeable difference between the homogeneous case and the inhomogeneous case, where the inhomogeneity works to raise the mean neutral fraction. In other words, it shows that the opacity effect is enhanced in an inhomogeneous medium. This effect obviously delays the end of reionization.

3.2   Uneven surface of reionization and anisotropies in CIB

The inhomogeneity in ionization structure reflects the level of density fluctuations. As a possible measure of such inhomogeneous reionization, we here tentatively assess the anisotropies in the cosmic infrared background (CIB), which is produced by Lyα photons emitted by radiative recombination. Of course, the accurate prediction for the anisotropies requires the precise treatment of the thermal history as well as the non-linear
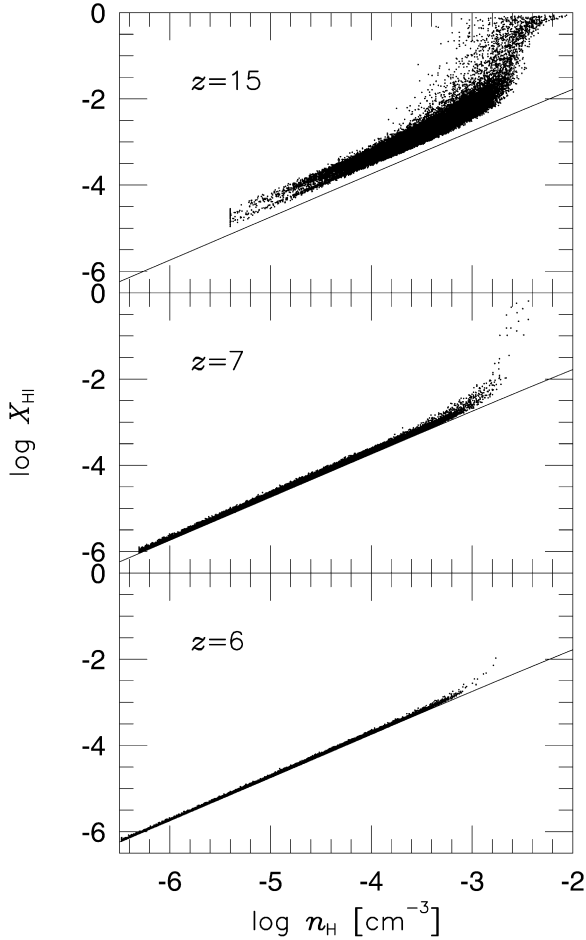
Figure 2. The local neutral fraction ($X_{\mathrm{H\,I}}$) versus the local hydrogen number density (n_{H}) at $z = 15$, 7 and 6. Each dot represents the local $X_{\mathrm{H\,I}}$ at a pixel. The prediction for the optically thin medium $X_{\mathrm{H\,I}} = 0.18 n_{\mathrm{H}} X_{\mathrm{e}}^2 J_{21}^{-1}$ is shown by a thin straight line. At $z = 15$ the numerical results significantly deviate from the optically thin prediction not only in self-shielded high-density regions but also in other whole regions including low-density regions. This is accounted for by the reduction of ionizing radiation owing to the collective opacity by numerous translucent regions. Such effects are not negligible also when strongly self-shielded regions mostly disappear at $z = 7$. At $z = 6$ almost all regions agree with the optically thin prediction. Thus the reionization is perfectly achieved. The present results show that the radiative transfer effects are still emergent even when the mean neutral fraction is at a level of 10^{-3}.

dynamics of density fluctuations. Thus, the present analysis gives just a crude measure, because the dynamics is incorporated by the Zel'dovich approximation and the isothermality is assumed here. (An accurate prediction can be made when 6D radiative transfer is coupled with 3D hydrodynamics.)

The behaviour of the background photons is governed by the cosmological radiative transfer equation including the time-derivative and the cosmic expansion (Baltz, Gnedin & Silk 1998). The Lyα lines have a large opacity at the rest frame, but the cosmological redshift allows the Lyα photons to propagate fairly freely. Assuming this, the redshifted Lyα photons which are originally emitted at z_{em} produce the intensity at the present epoch for $\nu = \nu_{\mathrm{Ly}\alpha}/(1 + z_{\mathrm{em}})$ as

$$I_\nu = \frac{c}{H_0} \frac{h}{4\pi} n_{\mathrm{H}}^2 X_{\mathrm{e}}^2 \alpha_{2p} (1 + z_{\mathrm{em}})^{-9/2}, \tag{6}$$
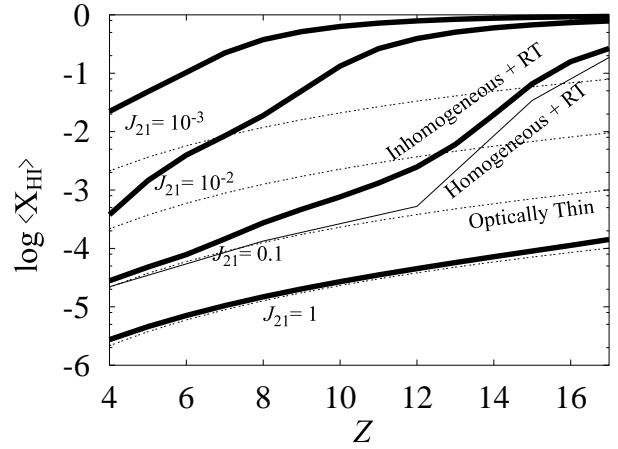
Figure 3. The spatial mean of the neutral hydrogen fraction is shown against redshifts for various UV intensities in the range of $10^{-3} \leqslant J_{21} \leqslant 1$. The thick solid curves are the results by the full radiative transfer calculations while thin dotted curves are the results under an assumption of an optically thin medium. For comparison the result of the radiative transfer calculation for a perfectly *homogeneous* medium are shown by a thin curve only for $J_{21} = 0.1$.

where c is the light speed, h is the Planck constant and α_{2p} is the recombination rate to $2p$ states of hydrogen (Baltz et al. 1998). This gives numerically

$$\nu I_\nu = 2.54 \times 10^{-14} h_{50}^{-1} X_{\mathrm{e}}^2 \Delta^2 \left(\frac{\Omega_{\mathrm{b}}}{0.05} \right)^2 (1 + z_{\mathrm{em}})^{1/2} \, \mathrm{W \, m^{-2} \, sr^{-1}}, \tag{7}$$

where Δ is the density contrast, $\Delta \equiv \rho/\langle \rho \rangle$. In Fig. 4, the maps of the emergent flux are shown for the emission from several redshifts and therefore for several wavelengths, i.e. $\lambda = 1.2 \, \mu\mathrm{m}$ $[(1 + z_{\mathrm{em}})/10]$. At $z = 15$, small angular-scale features are prominent owing to the fast growing small-scale fluctuations. Although the cosmic density is high at this epoch, the flux of the CIB is reduced because of the low ionization. At $z = 9$, larger angular scale patterns emerge and the flux is raised. At $z = 7$, the contrast of the CIB is enhanced owing to the growth of density fluctuations. At $z = 5$, since the universe is perfectly transparent, the anisotropies come purely from the difference of local densities.

In Fig. 5, the dependence on the wavelength of the mean flux $\langle \nu I_\nu \rangle$, the root-mean-square $\langle (\nu I_\nu)^2 \rangle^{1/2}$, and the cross-correlation $\langle (\nu I_\nu)_\theta (\nu I_\nu)_{\theta'} \rangle^{1/2}$ with $\theta - \theta' = 10$ arcsec are shown. For comparison, the results of the optically thin reionization are also plotted. It is obvious that the radiative transfer effects reduce the flux significantly until the universe is perfectly optically thin, i.e. $z \sim 6$ for $J_{21} = 0.1$ and $z \sim 4$ for $J_{21} = 0.01$. The reduction is more prominent in the case of $J_{21} = 0.01$. The peak flux around $z = 6$ for $J_{21} = 0.1$ turns out to be larger by a factor of ~ 3 than what is predicted in the *homogeneous* reionization. This is evidently the consequence of the growth of the density fluctuations. The behaviour of the intensity is understood as follows. When the density fluctuations are in the weakly non-linear stage ($z \gtrsim 6$), the volume fraction of overdense regions is roughly $\Delta^{-1}/2$. Hence, the fractional contributions to $\langle \Delta^2 \rangle$ are $\Delta^2 \cdot \Delta^{-1}/2 = \Delta/2$. Similarly, the contributions of underdense regions are estimated to be $\Delta/[2(2\Delta - 1)]$. Thus, the emission comes predominantly from the overdense regions. As a result, in the
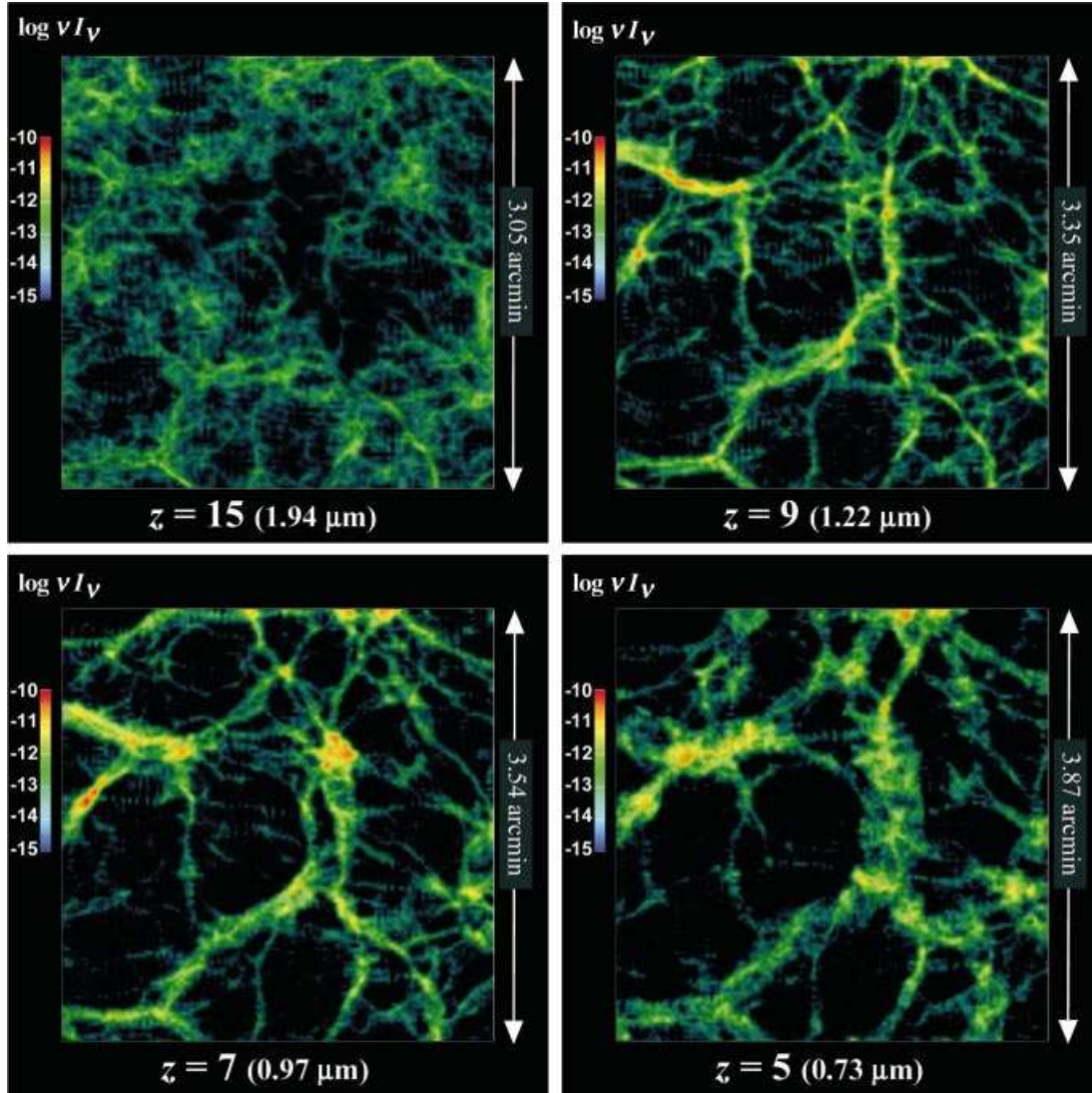
Figure 4. The flux map of the IR background radiation resulting from Lyα photons at several redshifts. The flux levels (νI_ν) in units of $W\,m^{-2}\,sr^{-1}$ are shown in logarithmic scales by colours according to the attached colour bar. The wavelength corresponds to the redshifts as $\lambda = 1.2\,\mu m[(1 + z_{em})/10]$. The flux is estimated on the slice at the midplane in the simulation box. It is noted that the angular scale of the simulation box is not sensitive to redshifts, owing to the cosmological angular-diameter distance. At $z = 15$, small angular-scale (several arcsec) features are prominent and the flux is reduced because of the low ionization. From $z = 9$ to $z = 7$, larger angular scale patterns emerge and the flux is raised owing to the growth of density fluctuations. At $z = 5$ the anisotropies come purely from the difference of local densities.

free-streaming regime for the redshifted Lyα photons, the mean flux gradually increases with time as $(1 + z_{em})^{-1/2}$ if the density contrast evolves as $\sim 1/(1 + z)$. On the other hand, the fractional contributions to $\langle \Delta^4 \rangle$ are $\Delta^4 \cdot \Delta^{-1}/2 = \Delta^3/2$ for overdense regions and $\Delta^3/[2(2\Delta - 1)^3]$ for underdense regions. Thus, the root-mean-square value (rms) increases with time as $(1 + z_{em})^{-1}$. The effects of the non-linearity make the dependence upon redshifts or wavelengths even steeper. Once isolated bound objects form at $z \lesssim 5$ (i.e. $\Delta = \text{const}$), both the mean flux and the rms decrease with time roughly as $(1 + z_{em})^{1/2}$ in accord with the naive expectation. It should be noted that the rms is larger by an order of magnitude at maximum than the mean flux. This reflects the level of the density contrast when the reionization is accomplished. However, we should pay attention to the fact that the Zel'dovich approximation breaks down in the highly non-linear regime. Therefore, the density distributions at $z < 5$ are less realistic. As a result, the assessment of CIB anisotropy is much

less reliable at $z < 5$ because it depends on the square of the density.

4   CONCLUSIONS

We have solved 6D radiative transfer in an inhomogeneous universe to elucidate the transfer effects on the cosmic reionization. For the present purpose, a variety of contrivances have been adopted in the radiative transfer solver. As a result, numerical simulations have shown that the radiative transfer effects resulting from the collective opacity by numerous translucent regions are significant even after the percolation epoch, and thereby the reionization in an inhomogeneous universe does not take place abruptly, but proceeds in a sluggish fashion. Consequently, the surface of reionization is highly uneven, although the surface is sharply edged if the universe is *homogeneous*. The recombination photons during the inhomogeneous reionization could produce the
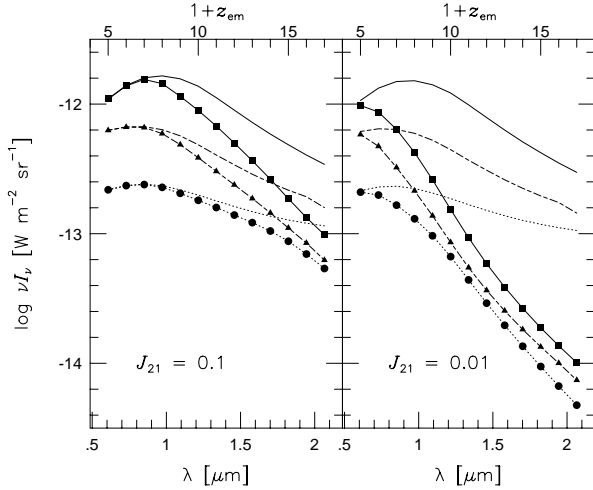
Figure 5. The wavelength dependence of the IR background radiation. The mean flux of the IR background $\langle \nu I_\nu \rangle$ (filled circles), the root-mean-square $\langle (\nu I_\nu)^2 \rangle^{1/2}$ (filled squares) and the cross-correlation at 10 arcsec $\langle (\nu I_\nu)_\theta (\nu I_\nu)_{\theta'} \rangle^{1/2}$ (filled triangles) are shown in cases of $J_{21} = 0.1$ as well as $J_{21} = 0.01$. Emission redshifts are also shown. Thin curves without symbols are the prediction in the optically thin limit. It turns out that the radiative transfer effects significantly reduce the flux until the universe is perfectly optically thin ($z \sim 6$ for $J_{21} = 0.1$ or $z \sim 4$ for $J_{21} = 0.01$). After bound objects form at $z \lesssim 5$, both the mean flux and the rms decrease with time as $(1 + z_{em})^{1/2}$.

cosmic near-IR background of $\sim 10^{-20}(\theta/\mathrm{arcmin})^2$ [W/m²] with a correlation scale of several arcmin. Such a level might be detected by forthcoming 8-m class IR space telescopes like the *Next Generation Space Telescope* (*NGST*) or the H2/L2 mission. If detected, the IR background anisotropies could provide precious information on density fluctuations and UV background intensity during the dark age.

In the present analysis, we have employed a highly simplified model for the ionizing sources, non-linear dynamics and thermal history. In that respect, this analysis is the first step for 3D cosmological radiation hydrodynamics. Since the reionization is not a prompt event as shown here, the practical reionization must proceed in close relation to the formation and evolution of luminous sources. Hence, to study such issues, more sophisticated analyses should be made, which include hydrodynamics and the formation of ionizing sources. This will be attacked in future research.

ACKNOWLEDGMENTS

REFERENCES

Abel T., Haehnelt M. G., 1999, ApJ, 520, L13

Abel T., Norman M. L., Madau P., 1999, ApJ, 523, 66
Bajtlik S., Duncan R. C., Ostriker J. P., 1988, ApJ, 327, 570
Baltz E. A., Gnedin N. Y., Silk J., 1998, ApJ, 493, L1
Barger A. J., Cowie L. L., Snaders D. B., 1999, ApJ, 518, L5
Bunn E. F., White M., 1997, ApJ, 480, 6
Ciardi B., Ferrara A., Governato F., Jenkins A., 2000a, MNRAS, 314, 611
Ciardi B., Ferrara A., Marri S., Raimondo G., 2000b, preprint (astro-ph/0005181)
Couchman H. M. P., Rees M. J., 1986, MNRAS, 221, 53
Dey A., Spinrad H., Stern D., Graham J. R., Chaffee F. H., 1998, ApJ, 498, L93
Fukugita M., Kawasaki M., 1994, MNRAS, 269, 563
Giallongo E., Cristiani S., D'Odorico S., Fontana A., Savaglio S., 1996, ApJ, 466, 46
Giroux M. L., Shapiro P. R., 1996, ApJS, 102, 191
Gnedin N. Y., 2000, ApJ, 535, 530
Gnedin N. Y., Ostriker J. P., 1997, ApJ, 486, 581
Gunn J. E., Peterson B. A., 1965, ApJ, 142, 1633
Haardt F., Madau P., 1996, ApJ, 461, 20
Haiman Z., Loeb A., 1997, ApJ, 483, 21
Haiman Z., Loeb A., 1998, ApJ, 503, 505
Haiman Z., Loeb A., 1999a, ApJ, 519, 479
Haiman Z., Loeb A., 1999b, ApJ, 521, L9
Iwasaki Y., 1998, Nucl. Phys. B (Proc. Suppl.), 60A, 246
Kitayama T., Ikeuchi S., 2000, ApJ, 529, 615
Kitayama T., Tajiri Y., Umemura M., Susa H., Ikeuchi S., 2000, MNRAS, 315, L1
Kunasz P., Auer L. H., 1988, J. Quant. Spectrosc. Radiat. Transfer, 39, 67
Madau P., 1995, ApJ, 441, 18
Madau P., 2000, Phys. Scr., 85, 156
Madau P., Haardt F., Rees M. J., 1999, ApJ, 514, 648
Milhalas D., Aver L. H., Milhalas B. R., 1978, ApJ, 220, 1001
Miralda-Escudé J., Rees M. J., 1998, ApJ, 497, 21
Miralda-Escudé J., Haehnelt M., Rees M. J., 2000, ApJ, 530, 1
Nakamoto T., 1999, in Miyama S. M., Tomisaka K., Hanawa T., eds, Numerical Astrophysics. Kluwer, Dordrecht, p. 375
Nakamoto T., Susa H., Umemura M., 1997, in Makino J., eds, New Horizon of Computational Science. Kluwer, Dordrecht, in press
Norman M. L., Paschos P., Abel T., 1998, Mem. Soc. Astron., It., 69, 455
Osterbrock D. E., 1989, Astrophysics of Gaseous Nebulae and Active Galactic Nuclei. University Science Books, Mill Valley, p. 12
Ostriker J. P., Gnedin N. Y., 1996, ApJ, 472, L63
Pei Y. C., 1995, ApJ, 438, 623
Razoumov A. O., Scott D., 1999, MNRAS, 309, 287
Sasaki S., Umemura M., 1996, ApJ, 462, 104
Schneider D. P., Schmidt M., Gunn J. E., 1991, AJ, 102, 837
Shapiro P. R., 1986, PASP, 98, 1014
Shapiro P. R., Giroux M. L., 1987, ApJ, 321, L107
Spinrad H., Stern D., Bunker A., Dey A., Lanzetta K., Yahil A., Pascarelle S., Fernández-Soto A., 1998, AJ, 116, 2617
Stern D., Spinrad H., Eisenhardt P., Bunker A. J., Dawson S., Stanford S. A., Elston R., 2000, ApJ, 533, L75
Stone J. M., Mihalas D., Norman M. L., 1992, ApJS, 80, 819
Susa H., Kitayama T., 2000, MNRAS, 317, 175
Tajiri Y., Umemura M., 1998, ApJ, 502, 59
Tegmark M., Silk J., 1994, ApJ, 423, 529
Thoul A. A., Weinberg D. H., 1996, ApJ, 465, 608
Umemura M., Ikeuchi S., 1984, Prog. Theor. Phys., 72, 47
Umemura M., Nakamoto T., Susa H., 1999, in Miyama S. M., Tomisaka K., Hanawa T., eds, Numerical Astrophysics. Kluwer, Dordrecht, p. 43
Valageas P., Silk J., 1999, A&A, 347, 1
Väth H. M., 1994, A&A, 284, 319
Weymann R. J., Stern D., Bunker A., Spinrad H., Chaffee F. H., Thompson R. I., Storrie-Lombardi L. J., 1998, ApJ, 505, L95
White S. D. M., Efstathiou G., Frenk C. S., 1993, MNRAS, 262, 1023

APPENDIX A: MULTIDIMENSIONAL RADIATIVE TRANSFER SOLVER

The radiation field is specified by the intensity $I(xyz; \theta\varphi\nu)$, which depends on six independent variables except for the time. The total amount of calculations is proportional to $N^3 \times N_\theta N_\varphi N_\nu$, where $N^3 N_\theta N_\varphi$ and N_ν are respectively the numbers of grids placed in the 3D cube zenith and azimuthal angles and frequencies. In our simulations we have used $N = 128$ $N_\theta = 128$ $N_\varphi = 128$ and $N_\nu = 6$. Here $N_\nu = 6$ is based upon the six-frequency approximation method, which is described in Appendix B in detail. As the problem requires a huge number of operations, we should make effective allowance for parallelization, which allows us to implement these 6D calculations on high-performance computers such as vector parallel computers or massively parallel computers. These kinds of effort to date have been hitherto few and far between (Väth 1994). In this Appendix, first we describe a basic numerical method to solve the radiative transfer equation. Secondly we show a way to decompose the problem. Thirdly we depict a new method we have devised to optimize the scheme for large parallel computers. Finally, the Λ iteration method which is employed to attain self-consistent solutions is described briefly.

A1 Short characteristics method

In order to solve the radiative transfer equation in a multi-dimensional space, we have adopted the so-called short characteristics (SC) method (Kunasz & Auer 1988; Stone et al. 1992). The computational cost in the SC method can be reduced compared with the direct ray tracing method by a factor of N, although the SC method is subject to numerical diffusion to some extent. The SC method is suitable for the transfer of diffuse radiation.

The solution of the radiative transfer equation is formally given by

$$I_\nu = I_\nu(0)\, e^{-\tau_\nu} + \int_0^{\tau_\nu} S_\nu(t) e^{-(\tau_\nu - t)}\, dt, \tag{A1}$$

where

$$\tau_\nu = \int_0^L (\kappa_{abs,\nu} + \kappa_{sca,\nu})\, dl \tag{A2}$$
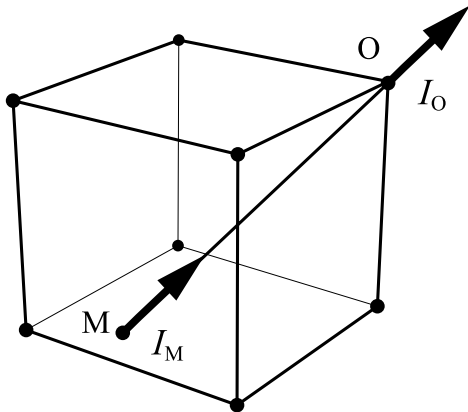

Figure A1. A segment of a ray in the *short characteristics* method is displayed. The depicted cube corresponds to a discretized cell in the configuration space. The quantities at a point M are obtained by interpolations using the values at the four nearest grid points.

and L is the length between a given point and a reference point. Both the absorption and the scattering contribute to the extinction, and also the scattering contributes to the source function S_ν as

$$S_\nu = \frac{\kappa_{sca,\nu}}{\kappa_{abs,\nu} + \kappa_{sca,\nu}} \int I_\nu\, d\Omega/4\pi. \tag{A3}$$

Since the source function S_ν depends on the intensity I_ν itself, some kind of iteration method is needed to obtain a self-consistent solution. We employ the so-called Λ iteration method, which is described later.

We discretize equations (A1) and (A2) along a ray. However, in general, the ray does not lie through spatial grid points based on the Cartesian coordinates in our calculations. In the SC method, to obtain the intensity I_O at a grid point O, upstream quantities at an intersection point M between the ray and a surface of a cell, i.e. intensity I_M, source function S_M, and extinction κ_M, are evaluated by interpolations (see Fig. A1). Next, using I_M, S_M and κ_M, the finite difference forms of equations (A1) and (A2) are given. If S and $\ln \kappa$ are assumed to be piecewise linear functions along the segment MO, then we have

$$I_O = I_M e^{-\tau} + S_M \frac{1 - e^{-\tau} - \tau e^{-\tau}}{\tau} + S_O \frac{\tau - 1 + e^{-\tau}}{\tau}, \tag{A4}$$

and

$$\tau = \int_M^O \kappa\, dl = L \frac{\kappa_O - \kappa_M}{\ln(\kappa_O/\kappa_M)}, \tag{A5}$$

where $\kappa \equiv \int (\kappa_{abs} + \kappa_{sca})\, d\nu$ is the extinction coefficient (Mihalas et al. 1978; Stone et al. 1992). It is worth noting that in the formula (A4), we do not have to care about optical thickness in advance. In other words, this method is valid for arbitrary optical thickness. Notice that the intensity on the upstream side should be calculated in advance of the intensity on the downstream side in order to satisfy the causality.

As for angular discretization, both the zenith angle θ ($0 \le \theta \le \pi$) and the azimuthal angle φ ($0 \le \varphi \le 2\pi$) are discretized uniformly. We use as many angular grid points as spatial grid points on a boundary surface (i.e. $N_\theta N_\varphi \simeq N^2$), in order to resolve all grid points on the boundary surface appropriately. This large number of angular grids allows us to solve the radiative transfer in a clumpy medium, where optically thick but geometrically small clumps are embedded in an optically thin medium. Thus, the present scheme is suitable for the problem of inhomogeneous reionization.

A2 Parallelization

In order to use a large parallel computer efficiently, we should carefully parallelize computations. In the case of radiative transfer calculations using the SC method, we can see that calculations for intensities with different angle (θ, φ) and frequency (ν) are independent of each other. Thus, the radiative transfer equation has a high potentiality of parallel computations by nature.

For the parallel computation, we should decompose the computational domain adequately. There are two typical ways of doing this for our calculations; one is angle decomposition and the other is space decomposition.

In the angle decomposition procedure, angular variables (θ, φ) are decomposed and assigned to each processing unit (PU), while no space variable is divided into any block. Each PU contains the whole three-dimensional space but calculates intensities only for

the angular grids that are assigned to the PU. This manner is rather easy to code, but with increasing N it requires larger local memories, so that computers feasible for this manner are limited.

In the space decomposition procedure, the configuration space (x, y, z) is divided into small blocks and assigned to each PU, while intensities with all angles and frequencies are calculated in each PU independently. One great advantage of this manner is that the required local memory is not so large. As what really we need in our reionization calculations is not the intensity itself but the integration of it over the solid angle, we do not have to store all values of intensities for all angles. After obtaining the value of the intensity for an angle, we add it to the integration and throw it away. We can thus reduce the total amount of memory tremendously. On the other hand, a disadvantage of the procedure is that the calculation sequence among PUs should be ordered carefully in order not to violate the causality. However, this disadvantage can be overcome by using *a multiple wavefront method* which we have devised. The method is described below. We can apply the space decomposition procedure to almost all parallel computers including not only vector parallel computers but also massively parallel computers, because the required local memory is not particularly large and the calculation sequence problem can be avoided by the wavefront method.

A3 Multiple wavefront method

In order to keep the calculation sequence appropriately and at the same time to use a parallel computer efficiently, we have devised a new method named the multiple wavefront (MWF) method. This is a method that controls the sequence of calculations among PUs and raises the degree of parallel computations.

To begin with, Cartesian coordinates are used to specify the three-dimensional configuration space and the space decomposition procedure is applied. For simplicity, let us decompose the configuration space into rectangular solid or cubic blocks with same size and same shape and order them in a three-dimensional way, although these conditions can be relaxed. We use the Cartesian PU-space coordinates (p_x, p_y, p_z), where $1 \leqslant p_x \leqslant P_x$, $1 \leqslant p_y \leqslant P_y$, $1 \leqslant p_z \leqslant P_z$, and P_x, P_y, P_z are the numbers of PUs
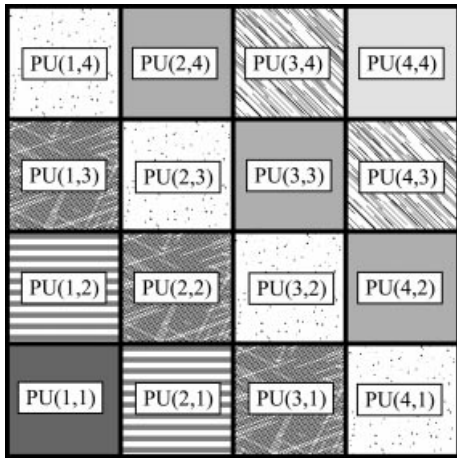

Figure A2. An example of the wavefront distribution in the two-dimensional PU space. In PUs having the same pattern, intensities with the same angular grid are calculated. Multiple wavefronts cover the whole PU space. Owing to this covering, the parallelization efficiency is raised high. For calculations presented in this paper, we employed the three-dimensional PU-space version of the MWF method.

in each PU-space dimension. The total number of PUs is $P_x P_y P_z$. It is easy and straightforward to generalize our method to two-dimensional and one-dimensional PU-space cases.

In the MWF method, we classify the angular grids into eight groups. A group to which an angular grid should belong is determined by examining whether the angular direction points towards the front ($\Delta x > 0$) or back ($\Delta x < 0$), right ($\Delta y > 0$) or left ($\Delta y < 0$), and up ($\Delta z > 0$) or down ($\Delta z < 0$). This classification is the basis of the calculation sequence management in the MWF method. An example of the wavefront distribution is shown in Fig. A2, although the PU-space is shown in a two-dimensional space for simplicity. For instance, when we calculate intensities, the angular grid of which is classified into the front–right–up direction group, we start our calculations from a PU that is in the back–left–bottom corner of the PU space [i.e. PU = $(1, 1)$] in order to satisfy the calculation sequence constraint. In the second step, we can continue calculation of intensities with that angular grid at PUs next to PU = $(1, 1)$, i.e. at PU = $(1, 2)$ and $(2, 1)$, by transferring the boundary values of the domain. In the following steps, we can continue calculations in the same way. Notice that PUs in which calculations of intensities with the same angular grid are carried out form a wavefront in the three-dimensional PU space. When we calculate a different direction group, we start calculations from a different PU which is suitable for the direction group. As is shown here, we can manage the calculation sequence among PUs using the angular direction groups.

In order to raise the degree of parallel computations, it should be noted that the calculation sequence among PUs is exactly the same among calculations if the angular grids belong to the same direction group. Since calculations of intensities with different angular grids can be carried out independently, we can calculate intensities with one angular grid in PUs on a wavefront in the PU space and at the same time intensities with another angular grid but in the same direction group in PUs on another wavefront different from the former wavefront. We can calculate $(P_x + P_y + P_z - 2)$ angular grids at a time, because $(P_x + P_y + P_z - 2)$ wavefronts can be present in the three-dimensional PU space. Owing to the presence of multiple wavefronts in the PU space, we can attain a high degree of parallel computations when the number of angular grids in a direction group is much larger than $P_x + P_y + P_z - 2$.

In order to evaluate the efficiency of parallel computation of the MWF method, let us define the parallelization efficiency f as the averaged ratio of the number of active PUs to the number of total PUs. The theoretical parallelization efficiency of the MWF method is estimated as

$$f = \frac{N_\theta N_\varphi / 8}{N_\theta N_\varphi / 8 + P_x + P_y + P_z - 3}. \tag{A6}$$

The expression (A6) is valid for the three-dimensional PU-space case, and those of two-dimensional and one-dimensional PU-space cases are given as $(N_\theta N_\varphi / 4)/(N_\theta N_\varphi / 4 + P_x + P_y - 2)$ and $(N_\theta N_\varphi / 2)/(N_\theta N_\varphi / 2 + P_x - 1)$, respectively. The parallelization efficiency f depends neither on the number of spatial grids N nor on the number of frequency grids N_ν. When we have $N_\theta = N_\varphi = 128$ grids and $P_x P_y P_z = 512$ ($P_x = P_y = P_z = 8$) PUs, the efficiency becomes $f = 0.990$, which is high enough. The loss of efficiency is attributed to the prologue and epilogue phases in which some PUs are waiting to calculate before the pass of the first wave or after the pass of the last wave.

We have confirmed that the MWF achieves very high efficiency for our calculations with the CP-PACS, which is a massively parallel computer with distributed local memories at the University of Tsukuba. The computational time with a fixed problem size per iteration step is almost proportional to the inverse of the number of PUs ($P_x P_y P_z$), when the size of the problem is not too small. In practice, there are some other factors that reduce the efficiency, such as inter-PU communications, barrier synchronizations, and so forth. For a typical calculation with $N = N_\theta = N_\varphi = 128$ and $N_\nu = 6$, it took about 100 h with 256 PUs of the CP-PACS to obtain a final solution.

A4   Λ iteration

In order to attain a solution in which the radiation field and the ionization state are consistent to each other, we employ the so-called Λ iteration. This method is one of the simplest methods that give a self-consistent solution when the source function S_ν depends on the intensity I_ν.

The procedure of the Λ-iteration method is quite simple. The ionization state can be determined if the UV radiation field is given with the ionization equilibrium condition. (In general, the density and the temperature are also needed to determine the ionization state. However, in our model, they are given and fixed using the Zel'dovich approximation and the isothermal assumption.) The radiation field can be obtained with the radiative transfer equation if the ionization state is provided. In the Λ iteration, the ionization calculation and the radiative transfer calculation are repeated alternately until those results converge on a consistent solution. We stop the iteration when the relative change of the mean intensity between iterations becomes less than 10^{-4}. The choice of this threshold did not lead to a significant change of our results.

APPENDIX B: THE SIX-FREQUENCY APPROXIMATION METHOD

Here, we demonstrate that the solution of the radiative transfer equation (4) at six frequencies gives the photoionization rates with fairly high accuracy. This method is based on the fact that the contribution to photoionization by a power-law continuum radiation can be readily integrated. The method is described in detail in the following section.

B1   Photoionization rates

The photoionization rates for H I, He I and He II are written in the form

$$k_{\mathrm{H\,I}} = \int_{\nu_1}^{\infty} \int \frac{I_\nu}{h\nu} \sigma_{\mathrm{H\,I}}(\nu) \, d\Omega \, d\nu, \tag{B1}$$

$$k_{\mathrm{He\,I}} = \int_{\nu_2}^{\infty} \int \frac{I_\nu}{h\nu} \sigma_{\mathrm{He\,I}}(\nu) \, d\Omega \, d\nu, \tag{B2}$$

$$k_{\mathrm{He\,II}} = \int_{\nu_3}^{\infty} \int \frac{I_\nu}{h\nu} \sigma_{\mathrm{He\,II}}(\nu) \, d\Omega \, d\nu, \tag{B3}$$

where ν_1, ν_2 and ν_3 are the Lyman-limit frequencies of H I, He I, and He II, and $\sigma_{\mathrm{H\,I}}(\nu)$, $\sigma_{\mathrm{He\,I}}(\nu)$, $\sigma_{\mathrm{He\,II}}(\nu)$ denote the photoionization cross-sections for H I, He I and He II, respectively. Those

photoionization cross-sections are given by

$$\sigma_{\mathrm{H\,I}}(\nu) = 6.30 \times 10^{-18} \left(\frac{\nu_1}{\nu}\right)^3 \mathrm{cm}^2, \tag{B4}$$

$$\sigma_{\mathrm{He\,I}}(\nu) = 7.42 \times 10^{-18} \left[1.66 \left(\frac{\nu_2}{\nu}\right)^{-2.05} - 0.66 \left(\frac{\nu_2}{\nu}\right)^{-3.05} \right] \mathrm{cm}^2, \tag{B5}$$

$$\sigma_{\mathrm{He\,II}}(\nu) = 1.575 \times 10^{-18} \left(\frac{\nu_3}{\nu}\right)^3 \mathrm{cm}^2 \tag{B6}$$

(Osterbrock 1989). Hence, in order to evaluate the photoionization rates, we need to evaluate the UV radiation intensity $I_\nu(\Omega, \nu)$ at each point.

B2   Frequency dependence of emissivity

The emissivity in the radiative transfer equation (4) is given in terms of the scattering term, although it originates from the recombination rates into various quantum states. Here, we go back to the original expression, so as to clarify the frequency dependence of the radiative transfer equation.

B2.1   H recombination

The energy of $\sim h\nu_1 + kT$ is emitted when an electron and a proton recombine on to the ground state. Thus, as far as the isothermal approximation at $T \sim 10^4$ K is concerned, the released energy at each recombination process is ~ 14.5 eV, which is close to the ionization energy 13.6 eV. Therefore, the recombination photons are confined to the narrow frequency band $\nu_1 \lesssim \nu \lesssim \nu_1 + \Delta\nu_T$, and the emissivity η_ν is configured as

$$\eta_\nu \Delta\nu_T \simeq \begin{cases} h\nu_1 \alpha_1 n_e n_p / 4\pi & \text{for } \nu_1 \leq \nu \leq \nu_1 + \Delta\nu_1, \\ 0 & \text{otherwise,} \end{cases} \tag{B7}$$

$$\Delta\nu_T = kT/h, \tag{B8}$$

where n_e and n_p are the number densities of electrons and protons, and α_1 is the direct recombination rate on to the ground state. This is an approximate expression, and the accurate emissivity is given by

$$\eta_\nu = 2 n_e n_p \frac{h^4 \nu^3}{m^3 c^2} \left(\frac{m}{2\pi kT}\right)^{3/2} \sigma_{\mathrm{H\,I}}(\nu) \exp\left(\frac{h\nu_1 - h\nu}{kT}\right)$$

$$\text{for } \nu > \nu_1, \tag{B9}$$

where m is the mass of an electron.

B2.2   He recombination

Similar to the hydrogen atom, the emissivities resulting from the recombination into the ground states of He I and He II are given by

He I :

$$\eta_\nu = \frac{1}{2} n_e n_{\mathrm{He\,II}} \frac{h^4 \nu^3}{m^3 c^2} \left(\frac{m}{2\pi kT}\right)^{3/2} \sigma_{\mathrm{He\,II}}(\nu) \exp\left(\frac{h\nu_2 - h\nu}{kT}\right)$$

$$\text{for } \nu > \nu_2, \tag{B10}$$

He II :

$$\eta_\nu = 2n_e n_{\text{He III}} \frac{h^4 \nu^3}{m^3 c^2} \left(\frac{m}{2\pi kT}\right)^{3/2} \sigma_{\text{He III}}(\nu) \exp\left(\frac{h\nu_3 - h\nu}{kT}\right)$$

$$\text{for } \nu > \nu_3. \tag{B11}$$

The emissivities are again localized in the frequency space, just above the Lyman limits of He I and He II, i.e. $h\nu_2 = 24.6\,\text{eV}$ and $h\nu_3 = 54.4\,\text{eV}$.

For He I and He II, the energy of bound–bound transition from an excited state to the ground state exceeds 13.6 eV. As a result, the emitted photon is able to ionize a hydrogen atom. Thus, we have to include such photons to assess the photoionization rates. These bound–bound transitions have the Doppler width $\Delta\nu_{D_i} \equiv \nu_i/c \times \sqrt{2kT/m}$, where ν_i is the line frequency listed below. We remark that this width is much narrower than $\Delta\nu_T$. The three major bound–bound transitions are

$h\nu_4 = 19.8\,\text{eV}$:

$$\eta_{\nu_4}\Delta\nu_{D_4} \simeq h\nu_4 \alpha_{\text{He I,B}} n_e n_{\text{He II}}/4\pi \times \tfrac{3}{4}, \tag{B12}$$

$h\nu_5 = 21.2\,\text{eV}$:

$$\eta_{\nu_5}\Delta\nu_{D_5} \simeq h\nu_5 \alpha_{\text{He I,B}} n_e n_{\text{He II}}/4\pi \times \tfrac{1}{6}, \tag{B13}$$

$h\nu_6 = 40.7\,\text{eV}$:

$$\eta_{\nu_6}\Delta\nu_{D_6} \simeq h\nu_6 \alpha_{\text{He II,B}} n_e n_{\text{He III}}/4\pi. \tag{B14}$$

Here, all of the recombination rates and the line specific factors are taken from Osterbrock (1989); $\alpha_{\text{He I,B}} = 2.73 \times 10^{-13}\,\text{cm}^{-3}\,\text{s}^{-1}$ and $\alpha_{\text{He II,B}} = 1.55 \times 10^{-12}\,\text{cm}^{-3}\,\text{s}^{-1}$.

In conclusion, the emissivity in H/He gas at $\sim 10^4\,\text{K}$ is confined in the narrow frequency bands ($\Delta\nu_T$ and $\Delta\nu_{D_i}$) around the three Lyman-limit frequencies and the three major lines. In other words, the emissivity is negligible in the rest of the wide range of frequencies.

B3 Evaluation of photoionization rates with the intensity at six frequencies

We have stated that in a wide range of the frequency space $\nu \geq \nu_1$ there is no source, except the vicinity of the Lyman limits of H/He and the helium recombination lines. Here, we divide the intensity I_ν into two parts, I_ν^{dir} and I_ν^{sca}. The former represents the photons which have never been scattered, and the latter represents the scattered photons. Notice that I_ν^{sca} becomes finite around the six frequencies $\nu_1, \cdots, \nu_5$, and ν_6.

The solution of radiative transfer equation for I_ν^{dir} is simply given by

$$I_\nu^{\text{dir}} = I_\nu^{\text{in}} \exp(-\tau_\nu), \tag{B15}$$

where I_ν^{in} is the incident intensity, which is assumed to be $I_\nu^{\text{in}} \propto \nu^{-1}$ in this paper.

B3.1 Pure H gas

In the case of a pure hydrogen gas (no helium), the optical depth τ_ν as a function of the frequency ν is expressed as a function of τ_{ν_1} as

$$\tau_\nu \simeq \tau_{\nu_1}(\nu_1/\nu)^3. \tag{B16}$$

Substituting equations (B4), (B15) and (B16) into equation (B1), the contribution from I_ν^{dir} to the photoionization rate for H I is

evaluated by

$$k_{\text{H I}}^{\text{dir}} = \int_{\nu_1}^\infty \int \frac{I_\nu^{\text{in}} e^{-\tau_\nu}}{h\nu} \sigma_{\text{H I}}(\nu)\, d\Omega\, d\nu.$$

This is analytically integrated over frequency to give

$$k_{\text{H I}}^{\text{dir}} = \frac{I_{\nu_1}^{\text{in}} \sigma_{\text{H I}}(\nu_1)}{h} \int \frac{1}{3\tau_{\nu_1}^{4/3}} \gamma(4/3, \tau_{\nu_1})\, d\Omega, \tag{B17}$$

where $\gamma(a, b)$ is the incomplete gamma function. In this way, we only need τ_{ν_1} to assess the contribution from the direct photons to the photoionization rate. The contribution from I_ν^{sca} could be evaluated by solving the radiative transfer equation at ν_1. The contribution to the photoionization rate becomes

$$k_{\text{H I}}^{\text{sca}} = \int_{\nu_1}^\infty \int \frac{I_\nu^{\text{sca}}}{h\nu} \sigma_{\text{H I}}(\nu)\, d\Omega\, d\nu, \tag{B18}$$

$$I_\nu^{\text{sca}} \simeq I_{\nu_1}^{\text{sca}} \exp\left(\frac{h\nu_1 - h\nu}{kT}\right), \tag{B19}$$

where $I_{\nu_1}^{\text{sca}} \equiv I_{\nu_1} - I_{\nu_1}^{\text{dir}}$, and I_{ν_1} is the solution of the radiative transfer equation at ν_1. In the equation (B19), it is assumed that I_ν^{sca} has the same frequency dependence as η_ν in equation (B7); this approximation is particularly accurate at the optically thick limit. Using the equation (B19), the integration over frequency in equation (B18) is carried out. Summing up contributions $k_{\text{H I}}^{\text{abs}}$ and $k_{\text{H I}}^{\text{sca}}$, we obtain the photoionization rate of a hydrogen atom. In this case, what we have to solve is the radiative transfer equation, only for $\nu = \nu_1$.

B3.2 H/He gas

Even when helium is present, the frequency integration of photoionization rates can be performed in a similar way to the pure hydrogen case, although we have to treat six frequencies. The procedure for the method is as follows.

(1) Solve the radiative transfer equation at the Lyman-limit frequencies of H I, He I, and He II.

(2) Solve the radiative transfer equations at three frequencies corresponding to the helium bound–bound transitions.

(3) Evaluate the photoionization rates originated from I_ν^{dir} using τ_{ν_1}, τ_{ν_2}, and τ_{ν_3}, which are obtained in step (1).

(4) Evaluate the photoionization rates originated from the scattered photons at the Lyman limits, with the assumption that $I_\nu^{\text{sca}} \propto \eta_\nu$.

(5) Evaluate the contribution from the three bound–bound lines to the photoionization rates, with the solution of step (2).

In step (3), we assess the photoionization rate originated from I_ν^{dir}, dividing the frequency space into three regions as follows:

(i) $\nu_1 < \nu \leq \nu_2$

$$\begin{aligned} k_{\text{H I}}^{\text{dir}}(1) &= \int_{\nu_1}^{\nu_2} \int \frac{I_\nu^{\text{dir}}}{h\nu} \sigma_{\text{H I}}(\nu)\, d\Omega\, d\nu, \\ &= \frac{I_\nu^{\text{in}} \sigma_{\text{H I}}(\nu_1)}{h} \int \frac{1}{3\tau_{\nu_1}^{4/3}} \\ &\quad \times \left\{ \gamma\left(4/3, \tau_{\nu_1}\right) - \gamma\left[4/3, \tau_{\nu_1}\left(\frac{\nu_1}{\nu_2}\right)^3\right] \right\} d\Omega. \end{aligned}$$

The integration over frequency can be carried out analytically in this range of frequencies.

(ii) $\nu_2 < \nu \leqslant \nu_3$

$$k_{\rm H\,I}^{\rm dir}(2) = \int_{\nu_2}^{\nu_3} \int \frac{I_\nu^{\rm dir}}{h\nu} \sigma_{\rm H\,I}(\nu)\, {\rm d}\Omega\, {\rm d}\nu,$$

$$= \frac{I_\nu^{\rm in}\sigma_{\rm H\,I}(\nu_1)}{h} \int\int_{x_2}^{x_3} x^{-5}$$

$$\times \exp[-\tau_{\nu_1}x^{-3} - \tau_{\nu_2}f(x)]\, {\rm d}x\, {\rm d}\Omega.$$

Here, $x_2 \equiv \nu_2/\nu_1, x_3 \equiv \nu_3/\nu_1$, and $f(x) \equiv 1.66(x/x_2)^{-2.05} - 0.66(x/x_2)^{-3.05}$. In this region, the integration cannot be performed analytically. Therefore, to evaluate the integration, we make use of a table of the integration as a function of τ_{ν_1} and τ_{ν_2}.

(iii) $\nu_3 < \nu$

$$k_{\rm H\,I}^{\rm dir}(3) = \int_{\nu_3}^{\infty} \int \frac{I_\nu^{\rm dir}}{h\nu} \sigma_{\rm H\,I}(\nu)\, {\rm d}\Omega\, {\rm d}\nu$$

$$= \frac{I_\nu^{\rm in}\sigma_{\rm H\,I}(\nu_1)}{h} \int\int_{x_3}^{\infty} x^{-5}$$

$$\times \exp[-(\tau_{\nu_1} + \tau_{\nu_3}x_3^3)x^{-3} - \tau_{\nu_2}f(x)]\, {\rm d}x\, {\rm d}\Omega.$$

In this region, a table which is a function of $\tau_{\nu_1} + \tau_{\nu_3}x_3^3$ and τ_{ν_2} is used to evaluate the integration over frequency.

The total contribution from $I_\nu^{\rm dir}$ to the H I photoionization rate becomes

$$k_{\rm H\,I}^{\rm dir} = k_{\rm H\,I}^{\rm dir}(1) + k_{\rm H\,I}^{\rm dir}(2) + k_{\rm H\,I}^{\rm dir}(3). \tag{B20}$$

Thus, we are able to evaluate the contribution to the photoionization rate of H I from $I_\nu^{\rm dir}$ with the optical depths τ_{ν_1}, τ_{ν_2}, and τ_{ν_3}.

We evaluate the photoionization rate contributed from the scattered photons (steps 4 and 5) by

$$k_{\rm H\,I}^{\rm sca} \simeq \int\int \left[\left(I_{\nu_1}^{\rm sca}\int_{\nu_1}^{\infty} {\rm e}^{\frac{(h\nu_1-h\nu)}{kT}} + I_{\nu_2}^{\rm sca}\int_{\nu_2}^{\infty} {\rm e}^{\frac{(h\nu_2-h\nu)}{kT}} \right. \right.$$

$$\left. + I_{\nu_3}^{\rm sca}\int_{\nu_3}^{\infty} {\rm e}^{\frac{(h\nu_3-h\nu)}{kT}} \right) \frac{\sigma_{\rm H\,I}(\nu)}{h\nu}\, {\rm d}\nu \right]\, {\rm d}\Omega$$

$$+ \int \left(\frac{I_{\nu_4}^{\rm sca}\sigma_{\rm H\,I}(\nu_4)}{h\nu_4}\Delta\nu_{D_4} + \frac{I_{\nu_5}^{\rm sca}\sigma_{\rm H\,I}(\nu_5)}{h\nu_5}\Delta\nu_{D_5} \right.$$

$$\left. + \frac{I_{\nu_6}^{\rm sca}\sigma_{\rm H\,I}(\nu_6)}{h\nu_6}\Delta\nu_{D_6} \right)\, {\rm d}\Omega. \tag{B21}$$

Here $I_{\nu_i}^{\rm sca} \equiv I_{\nu_i} - I_{\nu_i}^{\rm dir}$, and we assume that the scattered photons at the Lyman limits of H I, He I and He II have approximately the same frequency profile as the emissivities in equations (B7), (B10) and (B11). This approximation is already employed in equations (B18) and (B19) for pure hydrogen gas.

Summing up the all contributions (equations B20 and B21), we obtain the H I photoionization rate with good accuracy. The photoionization rates of He I and He II are also calculated in a similar way.
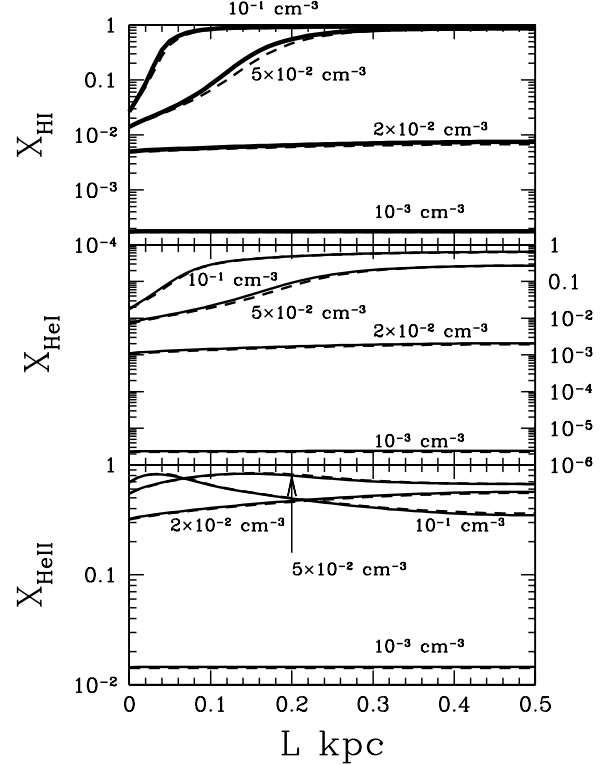

Figure B1. Fractions of H I, He I and He II in uniform slabs are plotted for various densities. The dashed curves are the results of the 700 frequency bins calculations. The solid curves are calculated by the six-frequency approximation. The horizontal axis denotes the physical length of the slab, measured from the outer boundary. The incident intensity at the Lyman limit, J_{21}, is unity. The number densities of the uniform slabs are $10^{-3}\,{\rm cm}^{-3}$, $2\times10^{-2}\,{\rm cm}^{-3}$, $5\times10^{-2}\,{\rm cm}^{-3}$ and $10^{-1}\,{\rm cm}^{-3}$. The thickness of the sheets is 1 kpc for all cases.

B4   Comparison with numerical calculation

The ionization state of a 1D slab exposed to the external UV radiation is calculated with two methods: the six-frequency approximation described above and a method employing 700 frequency bins for the frequency space. Fig. B1 shows the resultant fraction of H I, He I and He II at various locations in the slab for various densities. Solid curves and dashed curves represent the results obtained by the six-frequency approximation and by the numerical calculations with 700 frequency bins, respectively. It is seen that the results are in good agreement with each other. The difference between the two methods is maximal where the spatial gradient $({\rm d}X/{\rm d}L)$ in the fraction of each element is maximal. The relative difference in the location of the maximal gradient is less than 10 per cent for $X_{\rm H\,I}$, 6 per cent for $X_{\rm He\,I}$, or 2 per cent for $X_{\rm He\,II}$.

This paper has been typeset from a T$_{\rm E}$X/L$^{\rm A}$T$_{\rm E}$X file prepared by the author.